Electrochimica Acta 358 (2020) 136921

Contents lists available at ScienceDirect

Electrochimica Acta

journal homepage: www.elsevier.com/locate/electacta

In-situ reducing synthesis of MoP@nitrogen-doped carbon nanofibers as an anode material for lithium/sodium-ion batteries

Cuimei Fu[a], Hao Yang[a], Guofeng Feng[a], Lina Wang[a,*], Tianxi Liu[a,b,**]

[a] State Key Laboratory for Modification of Chemical Fibers and Polymer Materials, College of Materials Science and Engineering, Innovation Center for Textile Science and Technology, Donghua University, Shanghai 201620, China

[b] Key Laboratory of Synthetic and Biological Colloids, Ministry of Education, School of Chemical and Material Engineering, Jiangnan University, Wuxi 214122, China

ARTICLE INFO

Article history:
Received 6 June 2020
Revised 23 July 2020
Accepted 7 August 2020
Available online 12 August 2020

Keywords:
MoP
Nanofibers
Self-reduction phosphorization
Lithium/sodium-ion batteries

ABSTRACT

Transition metal phosphide anodes have received increasing attention for lithium/sodium-ion batteries due to their high theoretical capacities and apposite intercalation potential range. However, the mechanical stress induced dramatic volumetric expansion upon a conversion reaction mechanism has hindered the practical applications. Herein, we demonstrate a high performance anode of MoP@nitrogen-doped carbon nanofibers (MoP@NCNFs), which are prepared from an electrospinning method followed by an in-situ carbothermic self-reduction process. The well-crystallized MoP nanoparticles are uniformly distributed in the interweaving nanofibers, affording a conductive network for fast charge/ion transport and adequate buffer space for volumetric expansion. Benefit from the unique structure, the MoP@NCNFs synthesized at 800 °C delivers a reversible capacity of 840 mAh g^{-1} at 100 mA g^{-1} after 200 cycles. At 2 A g^{-1}, longer cycling upto 1300 cycles is achieved with a capacity of 377 mAh g^{-1} along with a Coulombic efficiency of 99% for Li storage. And a decent performance is also available for sodium storage. Quantitative kinetics analysis confirms that the charge storage behavior is governed by pseudocapacitance, especially at high rates (75.9% at 1 mV s^{-1}), boosting the high-rate lithium/sodium storage performance.

1. Introduction

To meet the growing energy demands, such as 5G mobile communication and hybrid electric vehicle requirements, enormous endeavors have been undertaken to efficiently utilize sustainable energy sources [1–3]. Lithium-ion batteries (LIBs) are currently the essential components of portable electronic devices and electric vehicles [4]. Sodium-ion batteries (SIBs) are a potential technique for large-scale energy storage owing to its similar electrochemical principles with LIBs and elemental abundance of sodium [5–7]. The most widely used graphite can deliver a theoretical specific capacity of 372 mAh g^{-1} for lithium storage. The ionic radius of the Na^+ (1.02 Å) is 34% larger than that of the Li^+ (0.76 Å) [8], which makes graphite cannot be used as a host material to accommodate Na^+ [9]. Considerable efforts have been focused on new-generation anode materials with higher capacity that can meet the requirements of both LIBs and SIBs.

Among various candidates of anode materials for Li/Na-ion batteries, that with an intercalation chemistry occupying one or fewer than one electron for per transition metal always give rise to a low capacity [10]. Alternatively, the anode materials based on a conversion reaction chemistry can deliver a much higher capacity [9,11]. Among which, transition metal phosphides show a broad perspective due to their higher specific capacities and apposite potential range (0.5–1 V) [12,13]. Such a potential range avoids the deposition potential of Li^+/Na^+ and averts the dendrite propagation [14]. MoP exhibits an electronic conductivity (10–100 S cm^{-1}) and a good electrochemical activity for LIBs/SIBs, which is very promising among the phosphides [15,16]. However, as other materials going through a conversion chemistry, MoP also suffers from mechanical stress induced volumetric expansion during the lithiation/delithiation processes. The resulted pulverization, aggregation and exfoliation of electrode materials would cause electrical contact losses, and thereby lead to reversible capacity fading during long-term cycling and poor rate capability [9].

The issue could be alleviated by particle nanosizing within conductive matrix. It is generally believed the nanoscale size would

* Corresponding author.
** Corresponding author at: State Key Laboratory for Modification of Chemical Fibers and Polymer Materials, College of Materials Science and Engineering, Innovation Center for Textile Science and Technology, Donghua University, Shanghai 201620, China.
E-mail addresses: linawang@dhu.edu.cn (L. Wang), txliu@dhu.edu.cn (T. Liu).

https://doi.org/10.1016/j.electacta.2020.136921
0013-4686/

provide sufficient ionic transport channels and relieve the volume strain [17]. And the conductive matrix would serve as efficient electron transporting geometries [18,19]. Nevertheless, the electrochemical performance is strongly dependent on the microstructure, which is determined by the synthesis route. In review of previous reports, there are two main strategies to synthesize the transition metal phosphides. One is solution-phase reaction, generally implemented in a high-boiling organic solvent with organic phosphines under oxygen free conditions at high temperature [20–22]. The other via a gas-solid reaction, which employed hypertoxic PH_3 (from pyrolytic hypophosphite) [23,24], PCl_3 [25], white or red phosphorus [26] acting as phosphorus sources. Although the much efforts have been made, the complex routes and the use of toxic chemicals make these methods infeasible to be scaled up. Recently, Wu et al. [27] and Wang et al. [28] prepared the phosphides by reducing metal orthophosphates directly under H_2 atmospheres. Although the simplified approach, the introduction of the extra H_2 gas would bring new safety issues for the practical applications.

With the aforementioned considerations, herein, we propose a facile and safe synthesis to fabricate MoP@nitrogen-doped carbon nanofibers (MoP@NCNFs) via an electrospinning method followed by a carbothermic in-situ self-reduction process. The obtained one-dimensional (1 D) nanofibers with uniformly distributed MoP nanoparticles are interconnected to form a three-dimensional (3 D) conductive network. The hierarchical construction acting as the electrochemical reaction chamber, not only prevents the aggregation of the MoP nanoparticles, but also accommodates their volume expansion upon phase transformation during the lithiation/delithiation processes. Therefore, the MoP@NCNFs benefits fast charge/ionic transport through the electrode/electrolyte interface. The increased pseudocapacitive contribution at higher current rates guarantees a superior electrochemical performance of MoP@NCNFs as Li-ion and Na-ion anode materials.

2. Experimental section

2.1. Synthesis of MoP@NCNFs

The electrospinning was carried out at room temperature. To prepare the precursor solution, typically, 0.4 mg hexaammonium heptamolybdate tetrahydrate ($(NH_4)_6Mo_7O_{24}{\cdot}4H_2O$, 99.0%, Sinopharm Chemical) and 0.3 mg ammonium phosphatedi basic ($(NH_4)_2HPO_4$, 99.99%, Aladdin) were dispersed in the mixed solvent of 10 mL deionized water (H_2O, 18.2 MΩ) and 5 mL ethyl alcohol (99.5%, Shanghai Lingfeng Chemical) by constant stirring to form a transparent solution. Then, 1 g polyvinylpyrrolidone (PVP, Sigma-Aldrich, M_w ~ 1,300,000) was added under continuous stirring for 12 h to form a homogeneous solution. Subsequently, the solution was electrospun under a voltage of 15 kV at a constant flow rate of 0.05 mL min^{-1} and a distance of 15 cm from the syringe to collector (ET2531, Beijing Ucalery Technology). After peeling off, the as-prepared films were dried at 80 °C overnight in a vacuum oven. Finally, the dired films were heated under N_2 atmosphere at 700, 800 or 900 °C for 3 h in a tube furnace with a heating rate of 5 °C min^{-1}, respectively. The obtained sample was donated as 700-MoP@NCNFs, 800-MoP@NCNFs, 900-MoP@NCNFs, respectively. In addition, a controlled MoP-free sample of nitrogen-doped carbon nanofibers (NCNFs) was prepared at the same condition with 800-MoP@NCNFs. And the bulk molybdenum phosphide (MoP, 99.5%, Shanghai Makclin Biochemical) was purchased for the electronic conductivity measurement and electrochemical tests.

2.2. Material characterizations

The morphology and microstructure were characterized with field emission scanning electron microscope (SEM, S-4800, HITACHI) equipped with energy dispersive spectrometer (EDS) and high-resolution transmission electron microscopy (TEM, JEM-2100F, JEOL). The crystal structures were measured by powder X-ray diffractometer (XRD, D/max-2550VB+/PC, X-ray, Rigalcu) with Cu Kα radiation at a current of 200 mA and voltage of 40 kV under a scan rate of 4° min^{-1}. The nitrogen adsorption-desorption isotherms were implemented on a Quadrasorb adsorption instrument (Quantachrome Instruments). The specific surface area was calculated according to the Brunauer-Emmett-Teller (BET) method. The pore size distribution was calculated from nitrogen sorption data using the nonlocal density functional theory (NLDFT) equilibrium model method. The valence state of the samples was analyzed by X-ray photoelectron spectrometer (XPS, Escalab 250Xi, Thermo Scientific) with Al Kα X-ray radiation. The content of carbon and nitrogen was determined by elemental analysis (VarioEL III). The electronic conductivity of the samples was measured by the four-probe method (RTS-8, Guangzhou Four Probe Tech.). Compressed powder pellets with a diameter of 12 mm diameter and a thickness of 0.3 mm were prepared for the electrical conductivity measurements.

2.3. Electrochemical measurements

CR2025 coin-type cells were used for the electrochemical measurements. For preparation of the electrodes, the MoP@NCNFs and NCNFs were mixed with super P carbon and poly(vinylidene fluoride) (8:1:1, wt%) in N-methyl-2-pyrrolidone (NMP, Shanghai Lingfeng Chemical). The homogeneous black-slurry was casted on a copper foil and then dried at 80 °C in a vacuum oven overnight to get the final electrode (12 mm in diameter). The average active material loading is around 3 mg cm^{-2}. To control the same active mass of MoP in the electrode, the bulk MoP mixed with super P carbon and poly(vinylidene fluoride) at a ratio of 66:24:10 (wt%) was prepared and measured in the same conditions. To assemble LIBs, Li foil (14 mm in diameter) was used as the counter electrode. The electrolyte was 1 M $LiPF_6$ in ethylene carbonate (EC)/dimethyl carbonate (DMC) (1:1, v/v). Polypropylene microporous film (celgard 2325, 25 μm thick, 16 mm in diameter) was severed as the separator. For SIBs, the counter electrode is Na foil. The electrolyte is 1 M $NaClO_4$ in ethylene carbonate (EC) and dimethyl carbonate (DMC) (1:1, v/v) in presence of 5% fluoroethylene carbonate (FEC) additive, and the glassfiber (Whatman, 260 μm thick, 16 mm in diameter) was utilized as the separator. The electrochemical measurements were performed at the room temperature of 25 °C. Cyclic voltammetry (CV) measurements were implemented on an electrochemical workstation (Arbin Instruments, USA) under 1.0–3.0 V. Electrochemical impedance spectra (EIS) were measured on a CHI660E electrochemical workstation. Galvanostatic charge–discharge curves were performed on a LAND CT2001A battery tester at different current densities within 0.01–3 V.

3. Results and discussion

3.1. Preparation and materials characterizations of MoP@NCNFs

The synthetic procedure of MoP@NCNFs involves a simple electrospinning and a subsequent thermal treatment, as illustrated in Fig. 1. In detail, the precursor fibers were produced by electrospinning a H_2O/ethanol solution of PVP, $(NH_4)_6Mo_7O_{24}{\cdot}4H_2O$ and $(NH_4)_2HPO_4$. The as-spun fibers were then thermally treated in a N_2 atmosphere to obtain MoP@NCNFs. PVP plays an important role in the synthetic procedure. Firstly, it provides the desirable rheological properties for electrospinning. Moreover, it serves as a carbon, CO and H_2 source, producing a strong reducing atmosphere

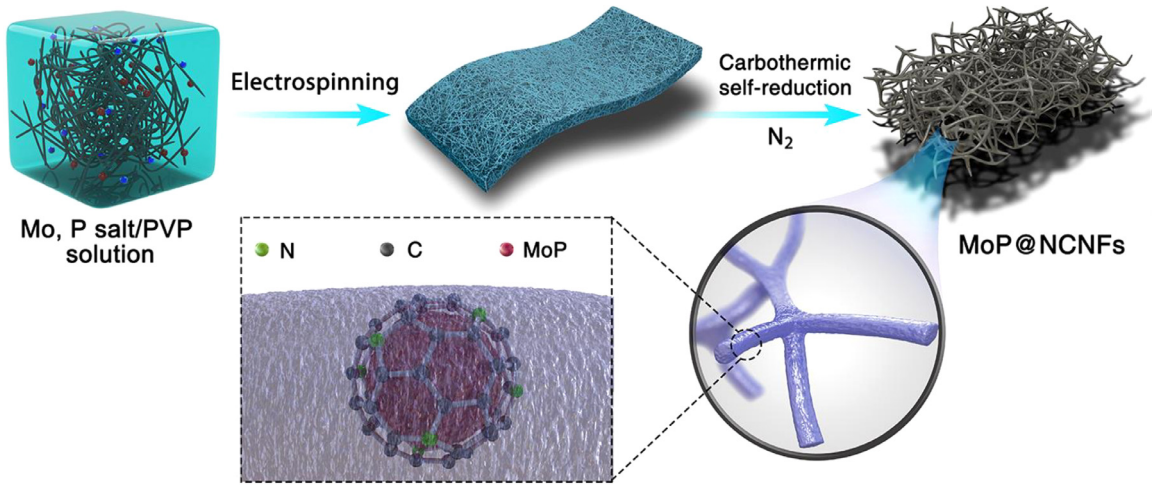

Fig. 1. Schematic illustration of the synthetic process of MoP@NCNFs.

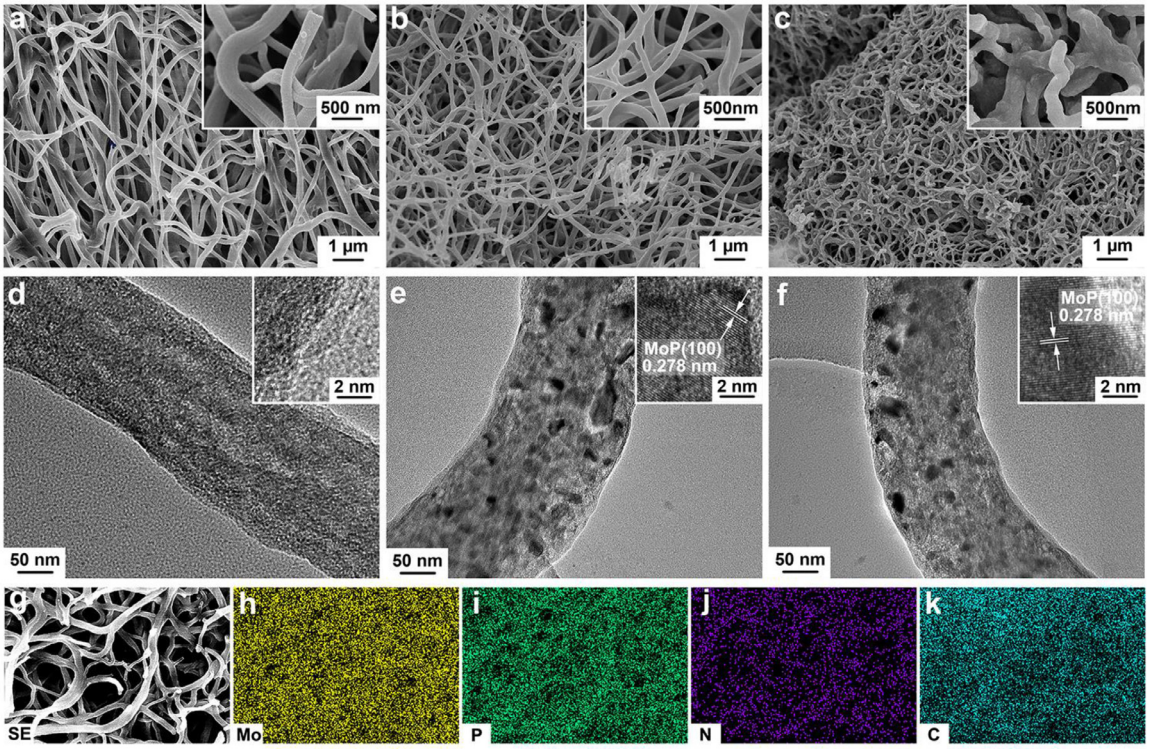

Fig. 2. SEM and TEM images of (a, d) 700-MoP@NCNFs, (b, e) 800-MoP@NCNFs, (c, f) 900-MoP@NCNFs and (g–k) corresponding elemental mappings of 800-MoP@NCNFs. The inset images are high magnifications.

during its pyrolysis. The Mo^{6+} and P^{5+} in the reactants are thereby reduced simultaneously to form MoP in the carbon nanofibers.

The morphology of the precursor and product fibers were examined by SEM firstly. The long, straight and smooth precursor fibers with a uniform diameter ca. 300 nm are interwoven into a network (Fig. S1). After the thermal treatment at different temperatures, the fibrous network can be maintained. However, the fibers become cincinnate like the naturally interconnected blood vessels. Such a phenomena should be resulted from the volatilization of H_2O/ethanol and the gas release from pyrolysis of PVP. It was also found that the microstructure of the products strongly depends on the synthesis temperature. The sample synthesized at 700 °C (700-MoP@NCNFs) exhibits an average diameter approximately 250 nm (Fig. 2a). The diameters of the nanofibers are decreasing with increasing the temperature, which are approximately 200 nm and 180 nm at 800 (800-MoP@NCNFs, Fig. 2b) and 900 °C (900-MoP@NCNFs, Fig. 2c), respectively. However, it can be seen that the 900-MoP@NCNFs exhibits more adhesive, agglomerated and irregular nanofibers than 800-MoP@NCNFs. The uniformly interconnected nanofibers of 800-MoP@NCNFs would provide more effective channels for fast ion diffusion and charge transfer. TEM were also conducted to further probe the microstructure structure of MoP@NCNFs (Fig. 2d–f). Crystalline MoP with clear lattice fringes (100) can be clearly seen in the nanofibers synthesized at 800 and 900 °C (inset in Fig. 2e and f). The MoP particles show a more homogeneous distribution in 800-MoP@NCNFs than in 900-MoP@NCNFs. Whereas, no lattice fringes of crystalline MoP appear in 700-MoP@NCNFs (inset in Fig. 2d), indicating MoP cannot successfully generated at 700 °C. The EDS analysis of 800-MoP@NCNFs depicts the well distribution of Mo, P, C, and N elements

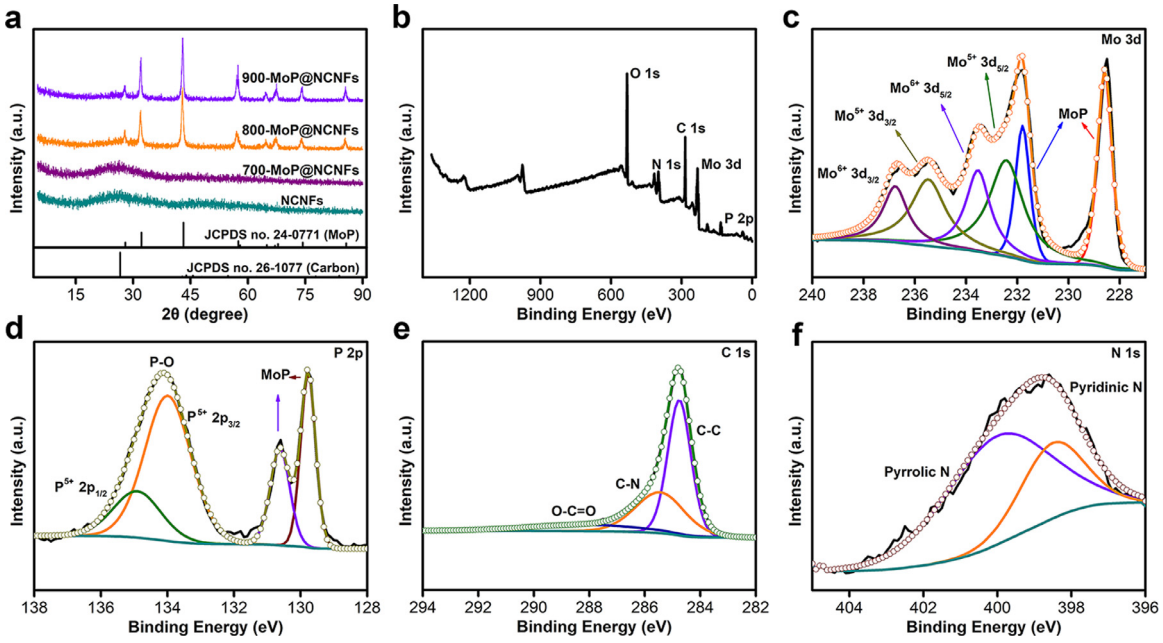

Fig. 3. (a) XRD patterns of MoP@NCNFs nanocomposites and standard PDF data of MoP (JCPDS no. 24-0771) and carbon (JCPDS no. 26-1077). The survey and high-resolution XPS spectra of 800-MoP@NCNFs nanocomposites: (b) the integrated XPS spectrum and the corresponding XPS spectrum of (c) Mo 3d, (d) P 2p, (e) C 1s, and (f) N 1s.

(Fig. 2g–k). The presence of N should be originated from the N atoms from pyrolytic PVP. N_2 adsorption-desorption isotherms and the pore size distribution analysis were carried out to further explore the porous structure and specific surface area of the 800-MoP@NCNFs. The BET specific surface area was calculated to be 31.35 m^2 g^{-1} (Fig. S2a). Benefit from the gas activation during carbonization, hierarchical mesopores and macropores are formed in the nanofibers (Fig. S2b). Such a unique structure should can provide abundant buffer space for volumetric expansion upon a conversion reaction and facilitate electrolyte access for fast transportation of ions.

XRD measurements were implemented to confirm the phase purity, as shown in Fig. 3a. With increasing the temperature, the peak of the crystalline are more sharp and intense. The diffraction patterns of the 800-MoP@NCNFs and 900-MoP@NCNFs exhibit several diffraction peaks of hexagonal MoP phase (JCPDS no. 24-0771), in which each Mo atom is trigonal-prismatically coordinated by six P atoms [29]. According to lattice parameters, the calculated grain size of MOP in 800-MoP@NCNFs is ca. 18.3 nm, which is smaller than that of ca. 23.8 nm in 900-MoP@NCNFs. The result further confirms the transformation of MoP crystal structure during the annealing at 800 or 900 °C. In contrast, the XRD pattern of 700-MoP@NCNFs shows an amorphous phase without peaks identified to crystalline MoP, further suggesting 700 °C is insufficient to generate crystalline MoP phase. Meanwhile, one peak centering at 26° belongs to (005) reflection of hexagonal carbon (JCPDS no. 26-1077), in good agreement with the XRD pattern of NCNFs. Elemental analysis suggests the C content is 27, 17 and 12 wt% in 700-MoP@NCNFs, 800-MoP@NCNFs and 900-MoP@NCNFs, respectively (Table S1). The respective N content is 3, 0.5 and 0.4 wt%, respectively. None N-containing compounds can be detected in the XRD patterns, indicating the N atoms are doped into the carbon nanofibers. N doping can dope an additional electronic pair into the delocalized π-system, which is beneficial to the electrical conductivity [30]. The synergistic effect of N doping and proper content carbon conductive network would lead to the enhanced electronic conductivity of nanosized MoP@NCNFs. The measured electronic conductivity of NCNFs, bulk MoP, 900-MoP@NCNFs and 800-MoP@NCNFs is 7.46, 12.67, 13.24 and 17.51 S cm^{-1}, respectively.

XPS was performed to evaluate the chemical composition and surface electronic state of the MoP@NCNFs. The presence of Mo, P, O, N and C have been observed by the survey XPS spectrum of 800-MoP@NCNFs (Fig. 3b). In the high-resolution Mo 3d spectrum (Fig. 3c), the two peaks at 231.88 and 228.56 eV are ascribed to MoP [31–33]. The peaks situated at 236.47 and 233.37 eV can be assigned to the $3d_{3/2}$ and $3d_{5/2}$ of Mo^{6+} [33,34], correspondingly. The two peaks located in 235.27 and 232.38 eV are corresponded to the $3d_{3/2}$ and $3d_{5/2}$ of Mo^{5+} [34,35], respectively. However, no significant impurities are detected from the XRD results in Fig. 3a, indicating the trace amount of Mo^{6+}/Mo^{5+}. The presence of high-priced Mo was previously ascribed to the surface oxidation of MoP when to be exposed in the ambient atmosphere [32,33]. However, the XRD patterns of the 800-MoP@NCNFs after storage for 2 years in air shows no datable changes (Fig. S3), indicating the stability of composite. Therefore, the coexistence of Mo^{6+}/Mo^{5+} should be more probably due to the instability of MoP during synthesis at high temperature. In Fig. 3d, the doublet 130.62 eV and 129.77 eV in the P 2p spectrum can be associated with P $2p_{1/2}$ and $2p_{3/2}$ of MoP [31], respectively. The P species at 134.89 and 133.98 eV are ascribed to P^{5+} $2p_{1/2}$ and $2p_{3/2}$, such as P bonded to O atoms in PO_4^{3-} and P_2O_5 [36,37]. The C 1s spectrum separated into three components at 284.8, 285.5 and 288.1 eV, which is attributed to graphitic C atoms, C–N and O–C=O [38], respectively (Fig. 3e). In the N 1s spectrum (Fig. 3f), the peak fitted with 400.0 and 398.5 eV are assigned to pyrrolic N [38] and pyridinic N [39], respectively. The XPS features of 900-MoP@NCNFs (Fig. S4) are almost the same with 800-MoP@NCNFs. However, no bands related to MoP are detected in the XPS spectrum of 700-MoP@NCNFs (Fig. S5), further verifying the XRD result in Fig. 3a.

3.2. Li^+ storage behavior of MoP@NCNFs

The Li^+ storage behavior of the MoP@NCNFs as-prepared at 800 and 900 °C was investigated with a Li-metal counter/reference electrode. CV test was measured within 0.01–3.0 V (vs. Li/Li^+) at a sweep rate of 0.1 mV s^{-1} (Fig. 4a). For the 800-MoP@NCNFs, a cathodic current peak centered at 0.86 V appears at the 1st cycle, which is assigned to the formation of a solid-electrolyte inter-

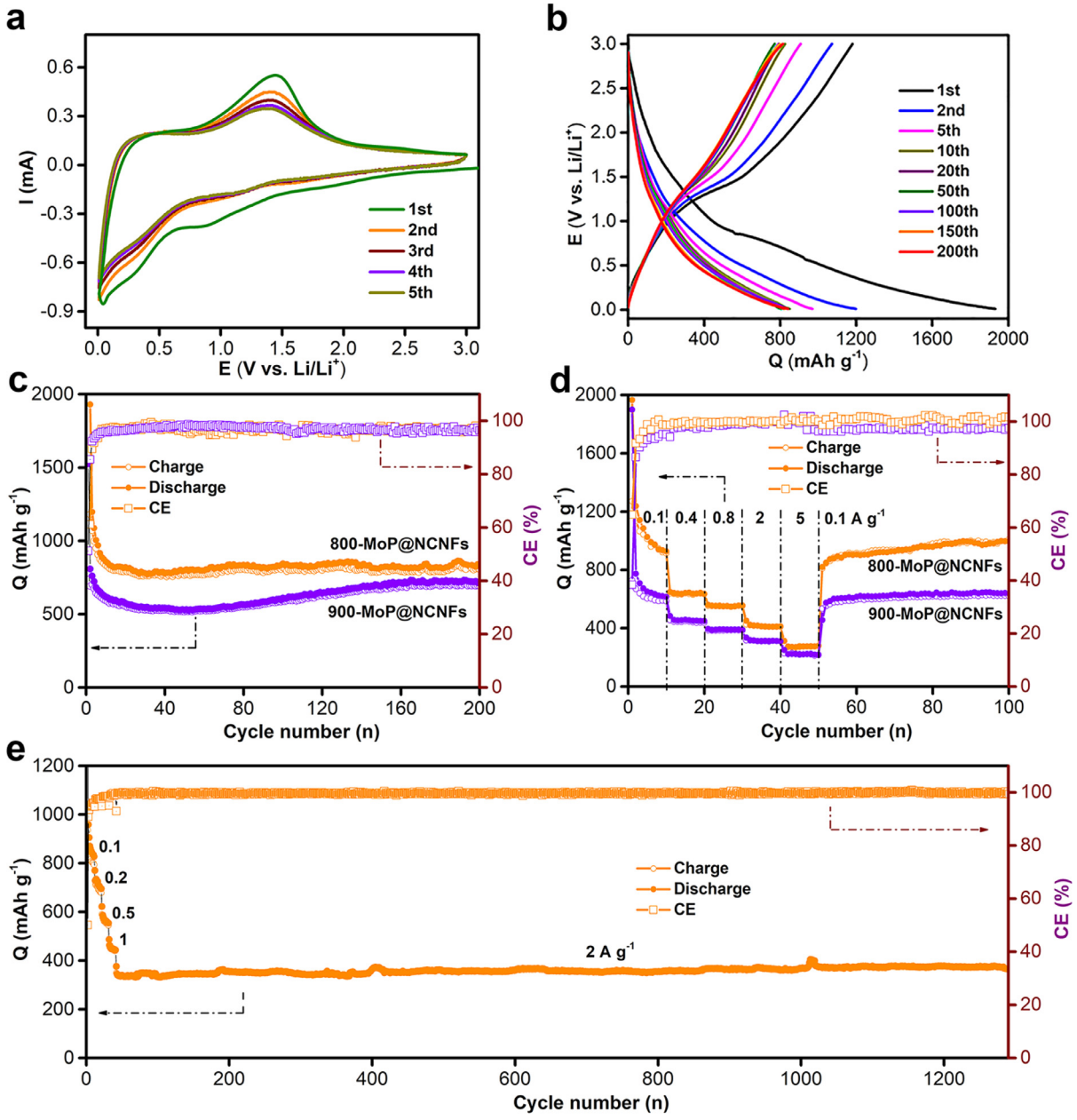

Fig. 4. (a) CV curves of the 800-MoP@NCNFs electrode at a scan rate of 0.1 mV s^{-1} in 0.01–3.0 V vs. Li/Li^+. (b) The charge–discharge profiles of the 800-MoP@NCNFs electrode at 0.1 A g^{-1}. (c) Cycling performance of the MoP@NCNFs electrode at a current density of 0.1 A g^{-1}. (d) Rate capability of MoP@NCNFs electrode at various current densities. (e) Longer-term cycling performance of the 800-MoP@NCNFs electrode at a current density of 2 A g^{-1}.

phase (SEI) [28]. Another peak below 0.5 V should be ascribed to the lithiation of MoP. In the reverse sweep, an obvious anodic peak appears at 1.4 V. In the following cycles, a weak peak at 1.12 V and a successive peak below 0.5 V can be clearly seen, indicating the lithiation of MoP is a step-wise process. The process is reversible as the broad anodic peak at 1.4 V shows repeatedly. The CV of 900-MoP@NCNFs demonstrates a similar feature (Fig. S6). The bulk MoP and NCNFs deliver an anodic/cathodic peak located at 1.17/0.65 V (Fig. S7a) and 1.18/1.15 V (Fig. S8a) for lithiation/delithiation of Li^+, respectively.

Fig. 4b shows the galvanostatic discharge–charge profiles of the 800-MoP@NCNFs at 100 mA g^{-1} within 0.01–3.0 V (vs. Li/Li^+). The charge–discharge profiles are in consist with the CV curves. In the 1st cycle, the discharge and charge capacities are 2144 and 1272 mAh g^{-1}, respectively, corresponding to a Coulombic efficiency (CE) of 60%. The loss of initial irreversible capacity is ascribed to the formation of the SEI layer on the electrode. In the initial 30 cycles, the specific capacities exhibit a slight decay. A gradual recovery of the capacity is observed in the following cycles (Fig. 4c), suggesting the formation of a stabilized SEI [40]. The reversible specific capacity is remained as high as 840 mAh g^{-1} upon 200 cycles, indicating a 71% retention of the discharge capacity from the 2nd cycle. The electrochemical performance of 5 samples include the error analysis (mean and standard deviation) are demonstrated in Fig. S9, which provide further evidence on the reliable performance. SEM images reveal that the interconnected fibrous structure of 800-MoP@NCNFs is well maintained after 200 cycles (Fig. S10). However, the same high cyclic stability and rate capability (Fig. 4d) are not achieved in terms of 900-MoP@NCNFs, which is mainly owing to the more uniform nanosized MoP and more effective interconnected channels for ion diffusion and charge transfer of 800-MoP@NCNFs. The much lower capacity and

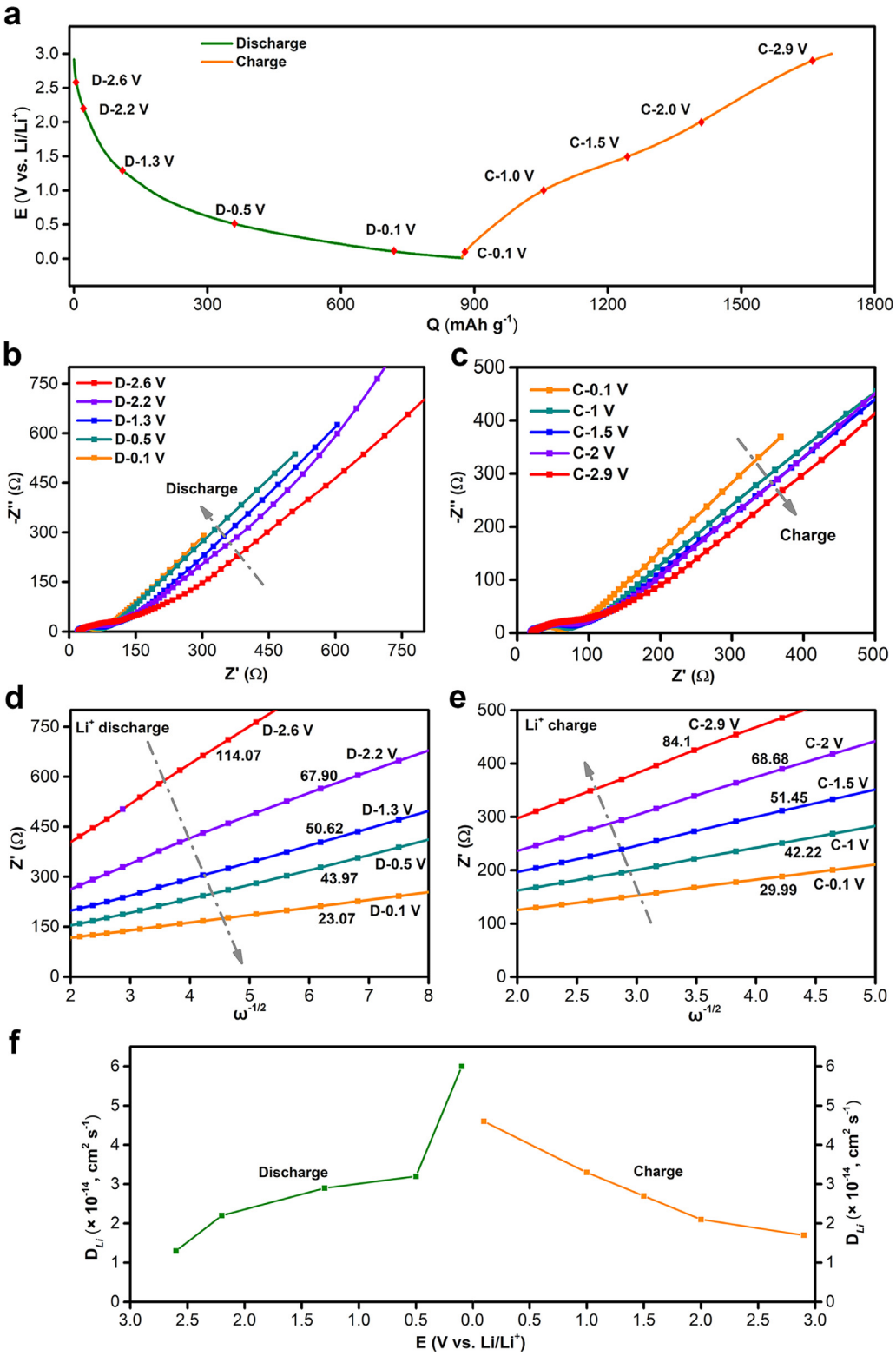

Fig. 5. The EIS analysis of 800-MoP@NCNFs: (a) discharge–charge profiles of 800-MoP@NCNFs, (b, c) Nyquist plots, (d, e) the liner relation of $\omega^{-1/2}$ vs. Z′ and (f) the D_{Li} value of different potential state.

rate performance of bulk MoP (Fig. S7b–d) further demonstrates the importance of a well-engineered microstructure. And the much higher cyclic and rate capability of MoP@NCNFs is achieved compared with NCNFs (Fig. S8b–d). The long-term cycling stability at fast charge–discharge rates is an important criterion for practical applications, which is evaluated at a current density of 2 A g^{-1} (Fig. 4e). Impressively, the 800-MoP@NCNFs exhibits 377 mAh g^{-1} upon 1300 cycles along with a CE of 99% at 2 A g^{-1}. Moreover, a capacity of 800 mAh g^{-1} after 800 cycles at 1 A g^{-1} and 236 mAh g^{-1} after 10000 cycles at 10 A g^{-1} are achieved (Fig. S11). The rise trend of the capacity after 400th at 1 A g^{-1} and 8000th cycles at 10 A g^{-1} should be related to the lithiation-induced re-

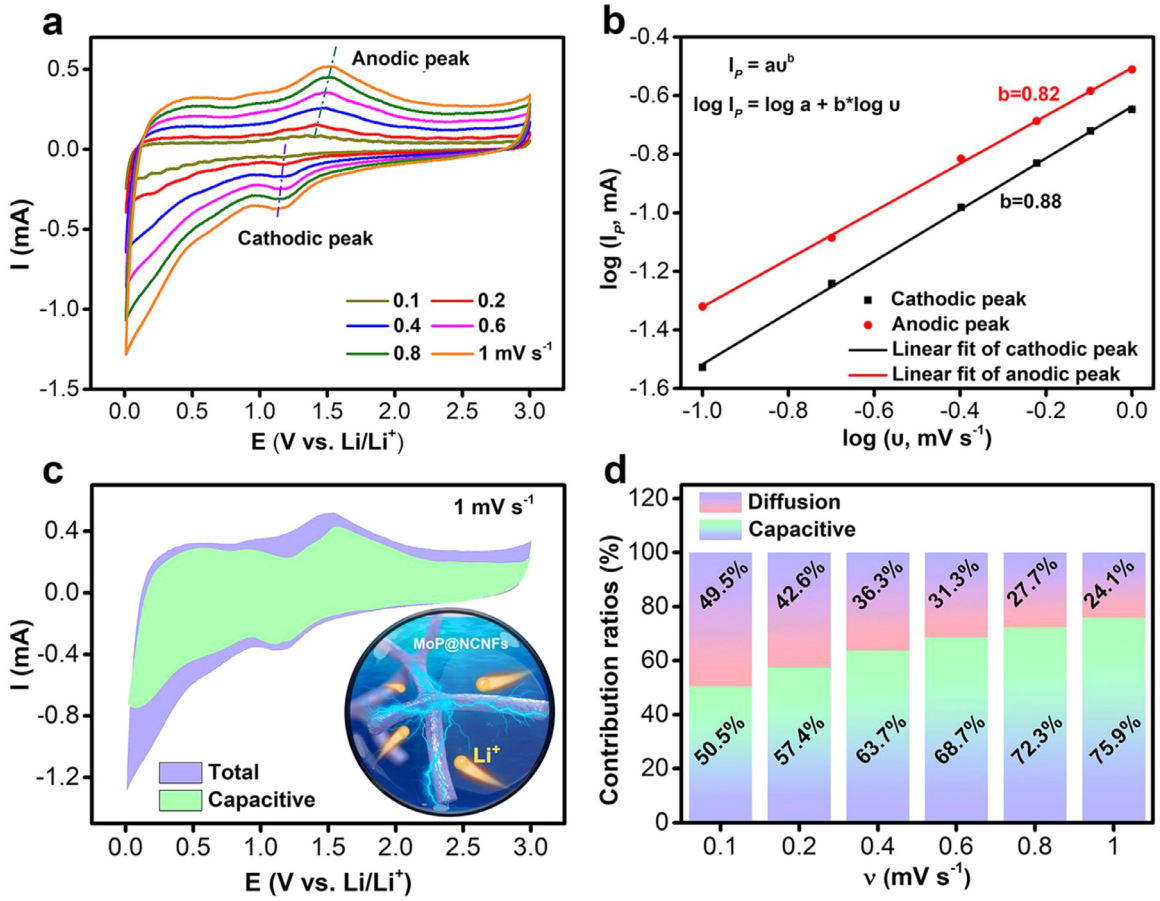

Fig. 6. (a) CV curves under various scan rates, from 0.1 to 1 mV s^{-1}. (b) The b value obtained by the slope of plots logν vs. logI_P under reduction and oxidation states. (c) Capacitive-controlled contribution to total current at a scan rate of 1 mV s^{-1}. (d) Current contribution ratio of capacitive and diffusion-controlled process at different scan rates.

activation and stabilization of MoP [40–42]. The increased accommodation behaviors of Li^+ cause the improved accessibility of Li^+ during the long cycles, further enhancing utilization of MoP. The performance is among the top results in comparison with the previously reported metal phosphide anode materials (Table S2).

EIS was carried out to get insight into the charge transfer kinetics of the MoP@NCNFs (Fig. S12a). The intercept to the real axis occurring at high frequency in each profile is index to the ohmic resistance (R_s). The component semicircle at high-to-medium frequency is related to the sum of the charge-transfer impedance (R_{ct}) and the contacting resistance (R_f). Whereas a slant line at low frequency is the Warburg impedance (R_w) [43]. The fitting Nyquist plots of the impedance spectroscopy are illustrated based on the equivalent circuit (Fig. S12b). As shown in Table S3, the fresh cell of 800-MoP@NCNFs exhibits a small R_{ct} of 178 Ω, which is further decreased to 46 Ω after 200 cycles. In contrast, the R_{ct} of 900-MoP@NCNFs is 221 Ω for fresh cell and 115 Ω after 200 cycles. The result further proves that the 800-MoP@NCNFs with an improved charge-transfer kinetics for Li-ion insertion and extraction.

The Li^+ storage mechanism was further investigated by ex-situ XRD and TEM analyses of the 800-MoP@NCNFs electrodes under evolutive voltage depths during the 20th cycle (Fig. S13a). The XRD patterns suggest MoP is gradually transformed to Li_3P during the lithiation process and the reaction is reversible during delithiation process (Fig. S13b). P_2O_5 and Li_2O impurities are introduced due to the atmospheric contaminations. The lattice fringes with a d-spacing of 0.278 nm assigned to the (100) planes of MoP (JCPDS no. 24-0771) were observed at the 3.0 V (Fig. S13c). In Fig. S13d, the lattice fringes appearing at 0.1 V are corresponded to the (−104) planes of Li_3P (JCPDS no. 04-0525). The result further proves the highly reversible conversion between MoP and Li_3P nanocrystals.

In order to assess the Li^+ diffusion at the electrode/electrolyte interface, the electrode at the marked voltage depths of the 200th cycle Fig. 5a) are investigated by the in-situ EIS (Fig. 5b and c). The diffusion coefficients of the lithium ion (D_{Li}) are evaluated according to Eqs. (1)–((3) [44,45]:

$$\omega = 2\pi f \tag{1}$$

$$Z' = R_s + R_{ct} + \sigma\omega^{-1/2} \tag{2}$$

$$D_{Li} = 0.5R^2T^2/A^2n^4F^4C^2\sigma^2 \tag{3}$$

where R is the gas constant (8.314 J mol^{-1} K^{-1}), σ is the Warburg coefficient, T is Kelvin temperature (293.15 K), A is the contact area of electrodes (1.13 cm^2), n is the electron number per molecule during the oxidization, F is faraday constant (96,485 C mol^{-1}) and C is the molar concentration of the Li^+. The values of σ are derived from the linear relation between Z′ (the real parts of impedance) and ω (angular frequency), corresponding values of D_{Li} are subsequently calculated from Eq. 3. The value of σ reduces from 114.07 Ω $s^{-1/2}$ at 1.68 V to 23.07 Ω $s^{-1/2}$ at 0.1 V during discharge (Fig. 5d), and then increases to 84.10 Ω $s^{-1/2}$ at a charge state of 2.9 V (Fig. 5e). Accordingly, the D_{Li} increases from 1.3 × 10^{-14} cm^2 s^{-1} (2.6 V) to 6.0 × 10^{-14} cm^2 s^{-1} (0.1 V) upon discharge, and decreases to 1.7 × 10^{-14} cm^2 s^{-1} (2.9 V) during charge (Fig. 5f and

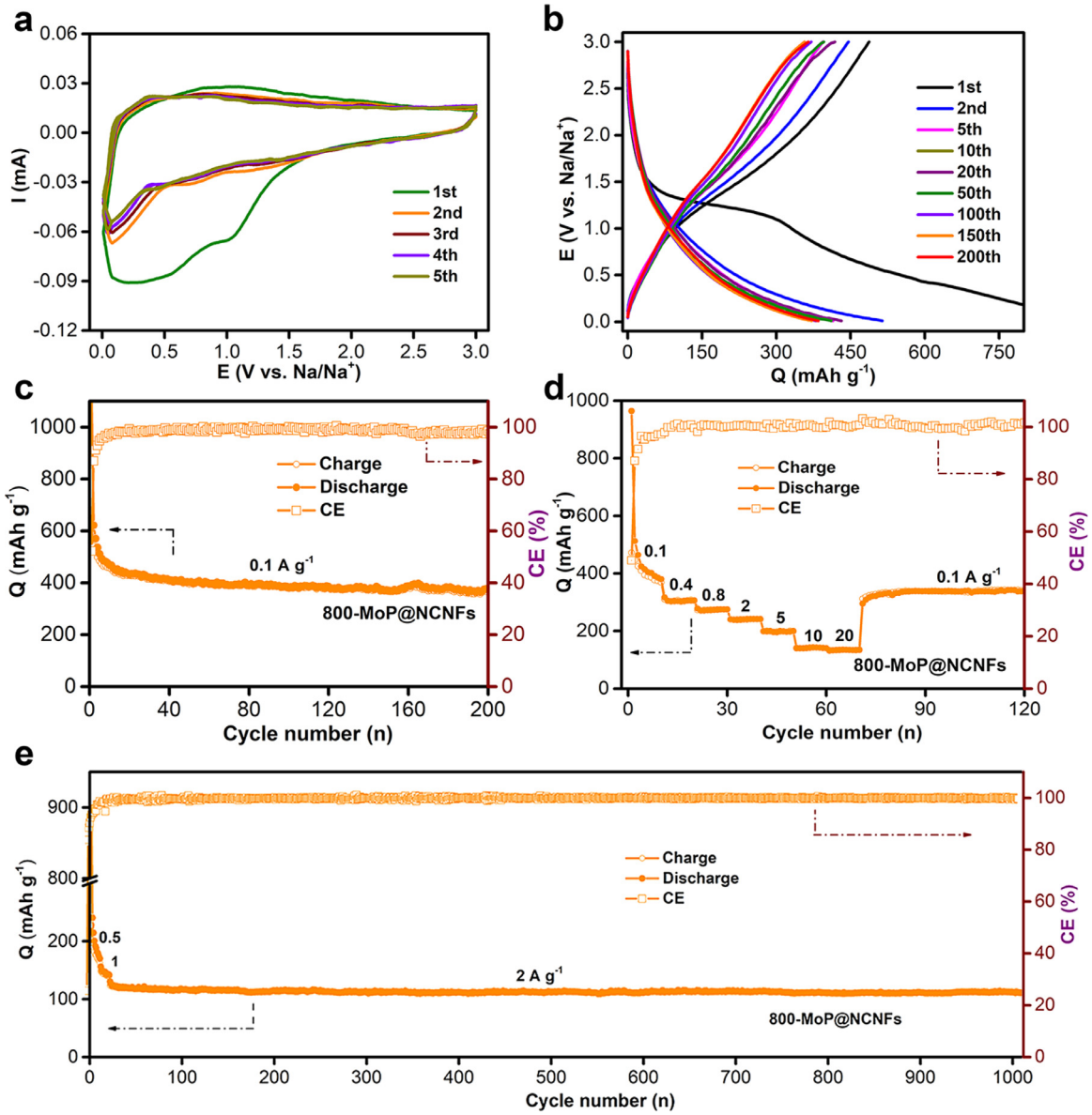

Fig. 7. The electrochemical performance of the 800-MoP@NCNFs electrode for sodium storage. (a) CV curves at a scan rate of 0.1 mV s^{-1} in 0.01–3.0 V vs. Na/Na^+. (b) The charge–discharge profiles at 0.1 A g^{-1}. (c) The corresponding cycling capability at a current density of 0.1 A g^{-1}. (d) Rate capability at various current densities. (e) Longer-term cycling performance at a current density of 2 A g^{-1}.

Table S4), suggesting the transformation from MoP to Li_3P would lead to a faster reaction kinetics.

To investigate the outstanding lithium storage behavior of 800-MoP@NCNFs, a detailed kinetics analysis is furthermore implemented herein. CV curves of the MoP@NCNFs electrode under different sweep rates ranging from 0.1 to 1.0 mV s^{-1} are obtained Fig. 6a). The charge-storage mechanism of MoP@NCNFs is explored according to the relationship between peak current (I_P) and sweep rate (ν) as following Eqs. (4) and (5) [46,47]:

$$I_P = a\nu^b \tag{4}$$

or reformulated as:

$$\log I_P = \log a + b\log\nu \tag{5}$$

where both a and b are adjustable parameters. The b-value demonstrates the dominated charge-storage mechanism, which exists two well-defined conditions: b = 0.5 and b = 1.0. Whereas b-value equals to 0.5, signifying the current is controlled by diffusion-controlled reaction. Instead, a b-value of 1 represents that the current is a capacitive response. Notably, by plotting the logν-log I_P curves Fig. 6b), the b-value of anodic and cathodic peak is determined to be 0.82 and 0.88, respectively. It is manifested that the electrochemical reaction kinetics of MoP@NCNFs is controlled by the pseudocapacitive behavior. Moreover, as a quantitative analysis of the capacitive and diffusion contribution in the MoP@NCNFs, the results are calculated according to the following Eqs. (6) and (7) [48]:

$$i = k_1\nu + k_2\nu^{1/2} \tag{6}$$

or reformulated as:

$$i/\nu^{1/2} = k_1\nu^{1/2} + k_2 \tag{7}$$

It is assumed that the measured current (i) at a fixed potential (V) is composed of pseudocapacitive behavior ($k_1\nu$) and diffusion-controlled contributions ($k_2\nu^{1/2}$). k_1 and k_2 constants can be determined by plotting $i/\nu^{1/2}$ versus $\nu^{1/2}$ to fit the slope (k_1) and the

intercept (k_2), respectively. From this procedure, the currents arising from diffusion-controlled and capacitive processes are able to be distinguished quantitatively. As shown in Fig. S14, the effects of the surface capacitive mechanism become eventually pronounced at higher sweep rates. The surface capacitive contribution accounts for a high value of 75.9% at 1 mV s^{-1} (Fig. 6c). The depressed diffusion and dominant capacitive contribution at higher rates are more clearly illustrated in Fig. 6d. The result suggests the rational structural engineering of metal phosphides holds promise to achieve a battery-level energy density and a capacitive-like cycling ability and rate capability.

3.3. Na^+ storage behavior of MoP@NCNFs

The Na^+ storage behavior of MoP@NCNFs was also investigated with a Na-metal counter/reference electrode. CV curves of 800-MoP@NCNFs in 0.01–3 V (vs. Na/Na^+) at a scan rate of 0.1 mV s^{-1} are shown in Fig. 7a, which shows a similar behavior with that of Li^+ storage. The main cathodic peak below 1 V attributes to the conversion of MoP to Na_3P. A broad anodic peak at 0.7–1.5 V corresponds to the reversible reaction [49]. CV curves of NCNFs exhibits an anodic peak at 0.1 V and a cathodic peak at 0.91 V assigned to the insertion/extraction of Na^+ in NCNFs (Fig. S15a). The discharge–charge profiles of 800-MoP@NCNFs within a voltage window of 0.01–3.0 V (vs. Na/Na^+) under 0.1 A g^{-1} are present in Fig. 7b. The initial discharge and charge capacity attain up to 1029 and 586 mAh g^{-1}, respectively. The sloping voltage profiles indicate a pseudocapacitive dominated Na^+ storage mechanism [50,51]. After a gradual capacity fading in the initial cycles, steady-state cycling are achieved (Fig. 7c). The reversible specific capacity is remained as 376 mAh g^{-1} after 200 cycles, much higher than NCNFs of 150 mAh g^{-1} for 200 cycles (Fig. S15b and c). The Na^+ storage performance of 5 samples include the error analysis (mean and standard deviation) are displayed in Fig. S16, which further verify the reliable performance. The rate performance of as-synthesized 800-MoP@NCNFs for Na^+ storage is shown in Fig. 7d. The reversible capacity maintains 404, 303, 273, 238 198, 143 and 135 mAh g^{-1} at the current densities of 0.1, 0.4, 0.8, 2.0, 5.0, 10 and 20 A g^{-1}, respectively. On-going from 20 to 0.1 A g^{-1}, a reversible capacity of 328 mAh g^{-1} recovers rapidly with a good cyclic stability, reflecting the MoP@NCNFs structural stability. However, a poor rate performance of 199, 157, 126, 94 and 72 mAh g^{-1} at 0.1, 0.4, 0.8, 2 and 5 A g^{-1}, respectively, is delivered for NCNFs (Fig. S15d). The long-term cyclic stability of 800-MoP@NCNFs are also tested at a high rate. As manifested in Fig. 7e, a reversible capacity of 117 mAh g^{-1} can be retained after 1000 cycles with 100% CE under 2 A g^{-1}. The performance can be comparable with other metal phosphide materials for Na^+ storage (Table S5). The diffusion coefficient of the lithium ion (D_{Na}) is also quantified to probe into the reaction kinetics of Na^+ storage (Fig. S17 and Table S6). The D_{Na} approaches 4.0×10^{-16} cm^2 s^{-1} at the full depth of discharge, further proving that the electrochemical performance of MoP can be greatly improved via building up the 3D architecture of MoP@NCNFs.

To explore the Na^+ storage mechanism, ex-situ XRD and TEM measurements were further implemented on the 800-MoP@NCNFs electrodes under different voltage depths during the 20th cycle (Fig. S18a). The XRD patterns demonstrate the reversible transformation of MoP to Na_3P during the discharge–charge process (Fig. S18b). The lattice fringes with a d-spacing of 0.278 nm corresponding to the (100) planes of MoP (JCPDS no. 24-0771) are identified at the OCV of 2.9 V (Fig. S18c). And the lattice fringes with a d-spacing of 0.309 nm assigned to the (102) planes of Na_3P (JCPDS no. 04-0764) can be clearly detected at 0.1 V (Fig. S18d). The result further verifies the highly reversible conversion reaction between MoP and Na_3P nanocrystals.

4. Conclusions

In summary, we proposed a facile and versatile synthetic strategy to fabricate high-performance MoP@NCNFs for LIBs/SIBs. The electrolyte readily penetrates into the interconnected conductive nanofiber network, providing a fast charge transport and promoting a pseudocapacitive behavior. Moreover, the unique structure significantly alleviates the active material pulverization and enhances the long-term cyclic performance. Therefore, the MoP@NCNFs present outstanding stability with a high reversible capacity for both Li^+ and Na^+ storage.

Declaration of Competing Interest

The authors declare that they have no known competing financial interests or personal relationships that could have appeared to influence the work reported in this paper.

CRediT authorship contribution statement

Cuimei Fu: Conceptualization, Methodology, Investigation, Data curation, Writing - original draft, Writing - review & editing, Visualization. **Hao Yang:** Formal analysis, Investigation, Data curation, Visualization. **Guofeng Feng:** Investigation, Data curation. **Lina Wang:** Methodology, Writing - original draft, Writing - review & editing, Supervision, Funding acquisition. **Tianxi Liu:** Supervision, Funding acquisition.

Acknowledgments

The authors acknowledge funding support from the Fundamental Research Funds for the Central Universities (2232018D3-02) and the Shanghai Scientific and Technological Innovation Project (18JC1410600).

Supplementary materials

Supplementary material associated with this article can be found, in the online version, at doi:10.1016/j.electacta.2020.136921.

References

[1] J.B. Goodenough, Energy storage materials: a perspective, Energy Storage Mater. 1 (2015) 158–161, doi:10.1016/j.ensm.2015.07.001.
[2] D. Larcher, J.M. Tarascon, Towards greener and more sustainable batteries for electrical energy storage, Nat. Chem. 7 (2015) 19–29, doi:10.1038/nchem.2085.
[3] Z.P. Cano, D. Banham, S. Ye, A. Hintennach, J. Lu, M. Fowler, Z. Chen, Batteries and fuel cells for emerging electric vehicle markets, Nat. Energy 3 (2018) 279–289, doi:10.1038/s41560-018-0108-1.
[4] M. Li, J. Lu, Z. Chen, K. Amine, 30 Years of lithium-ion batteries, Adv. Mater. 30 (2018) 1800561, doi:10.1002/adma.201800561.
[5] Y. Li, Y. Lu, C. Zhao, Y.-S. Hu, M.-M. Titirici, H. Li, X. Huang, L. Chen, Recent advances of electrode materials for low-cost sodium-ion batteries towards practical application for grid energy storage, Energy Storage Mater. 7 (2017) 130–151, doi:10.1016/j.ensm.2017.01.002.
[6] D. Kundu, E. Talaie, V. Duffort, L.F. Nazar, The emerging chemistry of sodium ion batteries for electrochemical energy storage, Angew. Chem. Int. Ed. 54 (2015) 3431–3448, doi:10.1002/anie.201410376.
[7] J. Ni, L. Li, J. Lu, Phosphorus: an anode of choice for sodium-ion batteries, ACS Energy Lett. 3 (2018) 1137–1144, doi:10.1021/acsenergylett.8b00312.
[8] L. Yang, Y.-E. Zhu, J. Sheng, F. Li, B. Tang, Y. Zhang, Z. Zhou, T-Nb_2O_5/C nanofibers prepared through electrospinning with prolonged cycle durability for high-rate sodium-ion batteries induced by pseudocapacitance, Small 13 (2017) 1702588, doi:10.1002/smll.201702588.
[9] P.K. Nayak, L. Yang, W. Brehm, P. Adelhelm, From lithium-ion to sodium-ion batteries: advantages, challenges, and surprises, Angew. Chem. Int. Ed. 57 (2018) 102–120, doi:10.1002/anie.201703772.
[10] K.T. Kim, G. Ali, K.Y. Chung, C.S. Yoon, H. Yashiro, Y.K. Sun, J. Lu, K. Amine, S.T. Myung, Anatase titania nanorods as an intercalation anode material for rechargeable sodium batteries, Nano Lett. 14 (2014) 416–422, doi:10.1021/nl402747x.
[11] J. Ni, X. Bi, Y. Jiang, L. Li, J. Lu, Bismuth chalcogenide compounds Bix (X=O, S, Se): Applications in electrochemical energy storage, Nano Energy 34 (2017) 356–366, doi:10.1016/j.nanoen.2017.02.041.

[12] F. Gillot, S. Boyanov, L. Dupont, M.L. Doublet, M. Morcrette, L. Monconduit, J.M. Tarascon, Electrochemical reactivity and design of NiP_2 negative electrodes for secondary Li-ion batteries, Chem. Mater. 17 (2005) 6327–6337, doi:10.1021/cm051574b.
[13] W.C. Records, S. Wei, A.M. Belcher, Virus-templated nickel phosphide nanofoams as additive-free, thin-film Li-ion microbattery anodes, Small 15 (2019) 1903166, doi:10.1002/smll.201903166.
[14] W. Liu, H. Zhi, X. Yu, Recent progress in phosphorus based anode materials for lithium/sodium ion batteries, Energy Storage Mater. 16 (2019) 290–322, doi:10.1016/j.ensm.2018.05.020.
[15] Y. Mi, W. Liu, X. Li, J. Zhuang, H. Zhou, H. Wang, High-performance Li–S battery cathode with catalyst-like carbon nanotube-MoP promoting polysulfide redox, Nano Res. 10 (2017) 3698–3705, doi:10.1007/s12274-017-1581-8.
[16] Y. Yin, L. Fan, Y. Zhang, N. Liu, N. Zhang, K. Sun, MoP hollow nanospheres encapsulated in 3D reduced graphene oxide networks as high rate and ultralong cycle performance anodes for sodium-ion batteries, Nanoscale 11 (2019) 7129–7134, doi:10.1039/C9NR00406H.
[17] Y. Lu, L. Yu, X.W.D. Lou, Nanostructured conversion-type anode materials for advanced lithium-ion batteries, Chem 4 (2018) 972–996, doi:10.1016/j.chempr.2018.01.003.
[18] Y. Feng, S. Chen, J. Wang, B. Lu, Carbon foam with microporous structure for high performance symmetric potassium dual-ion capacitor, J. Energy Chem. 43 (2020) 129–138, doi:10.1016/j.jechem.2019.08.013.
[19] Z. Liu, J. Wang, B. Lu, Plum pudding model inspired $KVPO_4F$@3DC as high-voltage and hyperstable cathode for potassium ion batteries, Sci. Bull. 65 (2020) 1242–1251, doi:10.1016/j.scib.2020.04.010.
[20] E.J. Popczun, J.R. McKone, C.G. Read, A.J. Biacchi, A.M. Wiltrout, N.S. Lewis, R.E. Schaak, Nanostructured nickel phosphide as an electrocatalyst for the hydrogen evolution reaction, J. Am. Chem. Soc. 135 (2013) 9267–9270, doi:10.1021/ja403440e.
[21] S. Cao, Y. Chen, C.-C. Hou, X.-J. Lv, W.-F. Fu, Cobalt phosphide as a highly active non-precious metal cocatalyst for photocatalytic hydrogen production under visible light irradiation, J. Mater. Chem. A 3 (2015) 6096–6101, doi:10.1039/C4TA07149B.
[22] Z. Huang, Z. Chen, Z. Chen, C. Lv, H. Meng, C. Zhang, $Ni_{12}P_5$ nanoparticles as an efficient catalyst for hydrogen generation via electrolysis and photoelectrolysis, ACS Nano 8 (2014) 8121–8129, doi:10.1021/nn5022204.
[23] X. Xu, J. Liu, Z. Liu, Z. Wang, R. Hu, J. Liu, L. Ouyang, M. Zhu, FeP@C nanotube arrays grown on carbon fabric as a low potential and freestanding anode for high-performance Li-ion batteries, Small 14 (2018) 1800793, doi:10.1002/smll.201800793.
[24] M. Pramanik, S. Tominaka, Z.L. Wang, T. Takei, Y. Yamauchi, Mesoporous semimetallic conductors: structural and electronic properties of cobalt phosphide systems, Angew. Chem. Int. Ed. 129 (2017) 13693–13697, doi:10.1002/ange.201707878.
[25] Z. Liu, S. Yang, B. Sun, X. Chang, J. Zheng, X. Li, A peapod-like CoP@ C nanostructure from phosphorization in a low-temperature molten salt for high-performance lithium-ion batteries, Angew. Chem. Int. Ed. 130 (2018) 10344–10348, doi:10.1002/ange.201805468.
[26] M. Sun, H. Liu, J. Qu, J. Li, Earth-rich transition metal phosphide for energy conversion and storage, Adv. Energy Mater. 6 (2016) 1600087, doi:10.1002/aenm.201600087.
[27] C. Wu, P. Kopold, P.A. van Aken, J. Maier, Y. Yu, High performance graphene/Ni_2P hybrid anodes for lithium and sodium storage through 3D yolk-shell-like nanostructural design, Adv. Mater. 29 (2017) 1604015, doi:10.1002/adma.201604015.
[28] X. Wang, P. Sun, J. Qin, J. Wang, Y. Xiao, M. Cao, A three-dimensional porous MoP@C hybrid as a high-capacity, long-cycle life anode material for lithium-ion batteries, Nanoscale 8 (2016) 10330–10338, doi:10.1039/C6NR01774F.
[29] Z. Sun, X.L. Wu, Z. Peng, J. Wang, S. Gan, Y. Zhang, D. Han, L. Niu, Compactly coupled nitrogen-doped carbon nanosheets/molybdenum phosphide nanocrystal hollow nanospheres as polysulfide reservoirs for high-performance lithium-sulfur chemistry, Small 15 (2019) 1902491, doi:10.1002/smll.201902491.
[30] Z.R. Ismagilov, A.E. Shalagina, O.Y. Podyacheva, A.V. Ischenko, L.S. Kibis, A.I. Boronin, Y.A. Chesalov, D.I. Kochubey, A.I. Romanenko, O.B. Anikeeva, T.I. Buryakov, E.N. Tkachev, Structure and electrical conductivity of nitrogen-doped carbon nanofibers, Carbon 47 (2009) 1922–1929, doi:10.1016/j.carbon.2009.02.034.
[31] X. Zhang, X. Yu, L. Zhang, F. Zhou, Y. Liang, R. Wang, Molybdenum phosphide/carbon nanotube hybrids as pH-universal electrocatalysts for hydrogen evolution reaction, Adv. Funct. Mater. 28 (2018) 1706523, doi:10.1002/adfm.201706523.
[32] Z. Wu, J. Wang, J. Zhu, J. Guo, W. Xiao, C. Xuan, W. Lei, D. Wang, Highly efficient and stable MoP-RGO nanoparticles as electrocatalysts for hydrogen evolution, Electrochim. Acta 232 (2017) 254–261, doi:10.1016/j.electacta.2017.02.146.
[33] M. Wei, B. Li, C. Jin, Y. Ni, C. Li, X. Pan, J. Sun, C. Yang, R. Yang, A 3D free-standing thin film based on N, P-codoped hollow carbon fibers embedded with MoP quantum dots as high efficient oxygen electrode for Li-O_2 batteries, Energy Storage Mater. 17 (2019) 226–233, doi:10.1016/j.ensm.2018.07.012.
[34] G. Zhang, T. Xiong, M. Yan, L. He, X. Liao, C. He, C. Yin, H. Zhang, L. Mai, α-MoO_{3-x} by plasma etching with improved capacity and stabilized structure for lithium storage, Nano Energy 49 (2018) 555–563, doi:10.1016/j.nanoen.2018.04.075.
[35] M. Vasilopoulou, A.M. Douvas, D.G. Georgiadou, L.C. Palilis, S. Kennou, L. Sygellou, A. Soultati, I. Kostis, G. Papadimitropoulos, D. Davazoglou, P. Argitis, The influence of hydrogenation and oxygen vacancies on molybdenum oxides work function and gap states for application in organic optoelectronics, J. Am. Chem. Soc. 134 (2012) 16178–16187, doi:10.1021/ja3026906.
[36] Y. Lu, J.P. Tu, Q.Q. Xiong, J.Y. Xiang, Y.J. Mai, J. Zhang, Y.Q. Qiao, X.L. Wang, C.D. Gu, S.X. Mao, Controllable synthesis of a monophase nickel phosphide/carbon (Ni_5P_4/C) composite electrode via wet-chemistry and a solid-state reaction for the anode in lithium secondary batteries, Adv. Funct. Mater. 22 (2012) 3927–3935, doi:10.1002/adfm.201102660.
[37] S. Liu, H. Xu, X. Bian, J. Feng, J. Liu, Y. Yang, C. Yuan, Y. An, R. Fan, L. Ci, Nanoporous red phosphorus on reduced graphene oxide as superior anode for sodium-ion batteries, ACS Nano 12 (2018) 7380–7387, doi:10.1021/acsnano.8b04075.
[38] X. Gao, B. Wang, Y. Zhang, H. Liu, H. Liu, H. Wu, S. Dou, Graphene-scroll-sheathed α-MnS coaxial nanocables embedded in N, S Co-doped graphene foam as 3D hierarchically ordered electrodes for enhanced lithium storage, Energy Storage Mater. 16 (2019) 46–55, doi:10.1016/j.ensm.2018.04.027.
[39] J. Zhou, Y. Wang, C. Zhang, Synthesis and electrochemical performance of core-shell $NiCo_2S_4$@nitrogen, sulfur dual-doped carbon composites via confined sulfidation strategy in a polydopamine nanoreactor, Compos. Commun. 12 (2019) 74–79, doi:10.1016/j.coco.2019.01.001.
[40] H. Kim, W. Choi, J. Yoon, J.H. Um, W. Lee, J. Kim, J. Cabana, W.-S. Yoon, Exploring anomalous charge storage in anode materials for next-generation Li rechargeable batteries, Chem. Rev. (2020), doi:10.1021/acs.chemrev.9b00618.
[41] H. Sun, G. Xin, T. Hu, M. Yu, D. Shao, X. Sun, J. Lian, High-rate lithiation-induced reactivation of mesoporous hollow spheres for long-lived lithium-ion batteries, Nat. Commun. 5 (2014) 4526–4533, doi:10.1038/ncomms5526.
[42] Y. Ma, U. Ulissi, D. Bresser, Y. Ma, Y. Ji, S. Passerini, Manganese silicate hollow spheres enclosed in reduced graphene oxide as anode for lithium-ion batteries, Electrochim. Acta 258 (2017) 535–543, doi:10.1016/j.electacta.2017.11.096.
[43] X. Miao, R. Yin, X. Ge, Z. Li, L. Yin, Ni_2P@ carbon core-shell nanoparticle-arched 3D interconnected graphene aerogel architectures as anodes for high-performance sodium-ion batteries, Small 13 (2017) 1702138, doi:10.1002/smll.201702138.
[44] X. Yang, A.L. Rogach, Electrochemical techniques in battery research: a tutorial for nonelectrochemists, Adv. Energy Mater. 9 (2019) 1900747, doi:10.1002/aenm.201900747.
[45] H. Zhang, P. Zong, M. Chen, H. Jin, Y. Bai, S. Li, F. Ma, H. Xu, K. Lian, In situ synthesis of multilayer carbon matrix decorated with copper particles: enhancing the performance of Si as anode for Li-ion batteries, ACS Nano 13 (2019) 3054–3062, doi:10.1021/acsnano.8b08088.
[46] V. Augustyn, J. Come, M.A. Lowe, J.W. Kim, P.-L. Taberna, S.H. Tolbert, H.D. Abruña, P. Simon, High-rate electrochemical energy storage through Li^+ intercalation pseudocapacitance, Nat. Mater. 12 (2013) 518–522, doi:10.1038/nmat3601.
[47] L. Wang, G. Yang, J. Wang, S. Wang, C. Wang, S. Peng, W. Yan, S. Ramakrishna, In situ fabrication of branched TiO_2/C nanofibers as binder-free and free-standing anodes for high-performance sodium-ion batteries, Small 15 (2019) 1901584, doi:10.1002/smll.201901584.
[48] J. Wang, J. Polleux, J. Lim, B. Dunn, Pseudocapacitive contributions to electrochemical energy storage in TiO_2 (anatase) nanoparticles, J. Phys. Chem. C 111 (2007) 14925–14931, doi:10.1021/jp074464w.
[49] Z. Huang, H. Hou, C. Wang, S. Li, Y. Zhang, X. Ji, Molybdenum phosphide: a conversion-type anode for ultralong-life sodium-ion batteries, Chem. Mater. 29 (2017) 7313–7322, doi:10.1021/acs.chemmater.7b02193.
[50] Y. Jiang, Y. Shen, J. Dong, S. Tan, Q. Wei, F. Xiong, Q. Li, X. Liao, Z. Liu, Q. An, L. Mai, Surface pseudocapacitive mechanism of molybdenum phosphide for high-energy and high-power sodium-ion capacitors, Adv. Energy Mater. 9 (2019) 1900967, doi:10.1002/aenm.201900967.
[51] Y. Gogotsi, R.M. Penner, Energy storage in nanomaterials–capacitive, pseudocapacitive, or battery-like? ACS Nano 12 (2018) 2081–2083, doi:10.1021/acsnano.8b01914.